



Measurements of jet multiplicity and jet transverse momentum in multijet events in proton-proton collisions at $\sqrt{s} = 13$ TeV

The CMS Collaboration

Abstract

Multijet events at large transverse momentum (p_T) are measured at $\sqrt{s} = 13$ TeV using data recorded with the CMS detector at the LHC, corresponding to an integrated luminosity of 36.3 fb^{-1} . The multiplicity of jets with $p_T > 50$ GeV that are produced in association with a high- p_T dijet system is measured in various ranges of the p_T of the jet with the highest transverse momentum and as a function of the azimuthal angle difference $\Delta\phi_{1,2}$ between the two highest p_T jets in the dijet system. The differential production cross sections are measured as a function of the transverse momenta of the four highest p_T jets. The measurements are compared with leading and next-to-leading order matrix element calculations supplemented with simulations of parton shower, hadronization, and multiparton interactions. In addition, the measurements are compared with next-to-leading order matrix element calculations combined with transverse-momentum dependent parton densities and transverse-momentum dependent parton shower.

Submitted to the European Physical Journal C

1 Introduction

The production of jets, which are reconstructed from a stream of hadrons coming from the fragmentation of energetic partons, is described by the theory of strong interactions, quantum chromodynamics (QCD). In proton-proton (pp) collisions, at leading order (LO) in the strong coupling α_s , two colliding partons from the incident protons scatter and produce two high transverse-momentum (p_T) partons in the final state. The jets that originate from such a process are strongly correlated in the transverse plane, and the azimuthal angle difference between them, $\Delta\phi_{1,2}$, should be close to π . However, higher-order corrections to the lowest order process will result in a decorrelation in the azimuthal plane, and $\Delta\phi_{1,2}$ will significantly deviate from π . These corrections can be due to either hard parton radiation, calculated at the matrix element (ME) level at next-to-leading order (NLO), or softer multiple parton radiation described by parton showers. In a recent approach [1], transverse-momentum dependent (TMD) parton densities are obtained with the parton-branching method [2, 3] (PB-TMDs). These PB-TMDs were combined with NLO ME calculations [4] supplemented with PB initial-state parton showers [5], leading to predictions where the initial-state parton shower is determined by the PB-TMD densities. Although $\Delta\phi_{1,2}$ is an inclusive observable, it is interesting for the theoretical understanding of the complete event to measure the multiplicity of jets in different regions of $\Delta\phi_{1,2}$ and the transverse momenta of the first four jets.

The azimuthal correlation in high- p_T dijet events was measured previously at: the Fermilab Tevatron in proton-antiproton collisions by the D0 Collaboration at $\sqrt{s} = 1.96$ TeV [6, 7]; and at the CERN LHC in pp collisions by both the ATLAS Collaboration at $\sqrt{s} = 7$ TeV [8] and the CMS Collaboration at $\sqrt{s} = 7, 8$, and 13 TeV [9–12].

In this paper, we describe new measurements of dijet events with rapidity $|y| < 2.5$ and with transverse momenta of the leading jet $p_{T1} > 200$ GeV and the subleading jet $p_{T2} > 100$ GeV. The multiplicity of jets with $p_T > 50$ GeV is measured in bins of p_{T1} and $\Delta\phi_{1,2}$. The jet multiplicity in bins of $\Delta\phi_{1,2}$ provides information on the $\Delta\phi_{1,2}$ decorrelation. The cross sections for the four leading jets are measured as a function of p_T of each jet, which can give additional information on the structure of the higher-order corrections.

This paper is organized as follows; in Section 2, a brief summary of the CMS detector and the relevant components is given. In Section 3, the theoretical models for comparison at detector level, as well as with the final results are described. Section 4 gives an overview of the analysis, with the event selection, data correction, and a discussion of the uncertainties. The final results and comparison with theoretical predictions are discussed in Section 5. The final section gives a summary.

2 The CMS detector and event reconstruction

The central feature of the CMS apparatus is a superconducting solenoid of 6 m internal diameter, providing a magnetic field of 3.8 T. Within the solenoid volume are silicon pixel and strip tracker detectors, a lead tungstate crystal electromagnetic calorimeter (ECAL), and a brass and scintillator hadron calorimeter (HCAL), each composed of a barrel part and two endcap sections.

Events of interest are selected using a two-tiered trigger system. The first level, composed of custom hardware processors, uses information from the calorimeters and muon detectors to select events at a rate of around 100 kHz within a fixed latency of about 4 μ s [13]. The second level, known as the high-level trigger (HLT), consists of a farm of processors running a version

of the full event reconstruction software optimized for fast processing, while reduces the event rate to around 1 kHz for data storage [14].

During the 2016 data-taking period, a gradual shift in the timing of the inputs of the ECAL first level trigger in the pseudorapidity region $|\eta| > 2.0$, also known as “prefiring”, caused some trigger inefficiencies [13]. For events containing a jet with $p_T > 100$ GeV, in the region $2.5 < |\eta| < 3.0$ the efficiency loss is 10–20%, depending on p_T , η , and the data-taking period. Correction factors were computed from data and applied to the acceptance evaluated by simulation.

The particle-flow (PF) algorithm [15] reconstructs and identifies each individual particle in an event, with an optimized combination of information from the various elements of the CMS detector. The energy of charged hadrons is determined from a combination of their momentum measured in the tracker and the matching ECAL and HCAL energy deposits, corrected for the response function of the calorimeters to hadronic showers. The energy of neutral hadrons is obtained from the corresponding corrected ECAL and HCAL energies.

The candidate vertex with the largest value of summed physics-object p_T^2 is taken to be the primary vertex (PV) of pp interactions as described in Section 9.4.1 of Ref. [16]. The physics objects are the jets, clustered using the jet finding algorithm [17, 18] with the tracks assigned to candidate vertices as inputs, and the associated missing transverse momentum.

Jets are reconstructed from PF objects, clustered using the anti- k_T algorithm [17, 18] with a distance parameter of $R = 0.4$. The jet momentum is determined as the vectorial sum of all particle momenta in the jet, and is found from simulation to be, typically, within 5 to 10% of the true momentum over the entire p_T spectrum and detector acceptance. Additional pp interactions within the same or nearby bunch crossings can contribute additional tracks and calorimetric energy deposits, increasing the apparent jet momentum. To mitigate this effect, tracks identified as originating from pileup vertices are discarded and an offset correction [19] is applied to correct for remaining contributions. Jet energy corrections are derived from simulation studies so that the average measured energy of jets becomes identical to that of particle-level jets. In situ measurements of the momentum balance in dijet, photon+jet, Z+jet, and multijet events are used to determine any residual differences between the jet energy scale (JES) in data and in simulation, and appropriate corrections are made [20]. Additional selection criteria are applied to each jet to remove jets potentially dominated by instrumental effects or reconstruction failures. The jet energy resolution (JER) amounts typically to 15–20% at 30 GeV, 10% at 100 GeV, and 5% at 1 TeV [20].

The missing transverse momentum vector \vec{p}_T^{miss} is computed as the negative vector sum of the transverse momenta of all the PF candidates in an event, and its magnitude is denoted as p_T^{miss} [21]. The \vec{p}_T^{miss} is modified to include corrections to the energy scale of the reconstructed jets in the event. Anomalous high- p_T^{miss} events can be due to a variety of reconstruction failures, detector malfunctions, or noncollision backgrounds. Such events are rejected by event filters that are designed to identify more than 85–90% of the spurious high- p_T^{miss} events with a mistagging rate less than 0.1% [21].

A more detailed description of the CMS detector, together with a definition of the coordinate system used and the relevant kinematic variables, can be found in Ref. [22].

3 Theoretical predictions

Theoretical predictions from Monte Carlo (MC) event generators at LO and NLO are used for comparison with measurements of the jet multiplicities as well as with the p_T spectra in multijet final states.

We use the following predictions at LO:

- PYTHIA8 [23] (version 8.219) simulates LO $2 \rightarrow 2$ hard processes. The parton shower is generated in a phase space ordered in transverse momentum and longitudinal momentum of the emitted partons, and the colored strings are hadronized using the Lund string fragmentation model. The CUETP8M1 [24] tune (with the parton distribution function (PDF) set NNPDF2.3LO [25]) gives the parameters for multiparton interactions (MPI).
- HERWIG++ [26] (version 2.7.1) simulates LO $2 \rightarrow 2$ hard processes. The emitted partons in the parton shower follow angular ordering conditions, and the cluster fragmentation model is used to transform colored partons into observable hadrons. The CUETHppS1 [24] tune (with the PDF set CTEQ6L1 [27]) is applied.
- MADGRAPH5_aMC@NLO [4] (version 2.3.3) event generator, labeled MADGRAPH+PY8, is used in the LO mode, with up to four noncollinear high- p_T partons included in the ME, supplemented with parton showering and multiparton interactions using PYTHIA8 with the CUETP8M1 tune and merged according to the k_T -MLM matching procedure [28] with a matching scale of 10 GeV.
- MADGRAPH5_aMC@NLO [4] (version 2.6.3) event generator, labeled MADGRAPH+CA3, is used in the LO mode to generate up to four noncollinear high- p_T partons included in the ME. We use the TMD merging [29] procedure for combining the TMD parton shower with the ME calculations. The NLO PB-TMD set 2 [1] with $\alpha_S(m_Z) = 0.118$ is used. The inclusion of the transverse momentum k_T and initial-state PB-TMD parton shower is performed with CASCADE3 [5] (version 3.2.3). The initial-state parton shower follows the PB-TMD distribution, and has no free parameters left. The final-state radiation (since not constrained by TMDs) as well as hadronization is performed with PYTHIA6 (version 6.428) [30] with an angular ordering veto imposed. A merging scale value of 30 GeV is used, since it provides a smooth transition between ME and PS computations. MPI effects are not simulated.

At NLO in the strong coupling, different theoretical predictions are used. The factorization and renormalization scales are set to half the sum over the scalar transverse momenta of all produced partons, $1/2 \sum H_T$. The uncertainty bands of the NLO predictions are determined from the variation of the factorization and renormalization scales by a factor of two up and down, avoiding the largest scale differences.

- MADGRAPH5_aMC@NLO [4] (version 2.6.3) interfaced with PYTHIA8 (version 8.306), labeled MG5_aMC+Py8 (jj), is used with MEs computed at NLO for the process $pp \rightarrow jj$. The NNPDF 3.0 NLO PDF set [31] is used and $\alpha_S(m_Z)$ is set to 0.118. This calculation uses the CUETP8M1 tune to study the effect of multiparton interactions.
- MADGRAPH5_aMC@NLO [4] (version 2.6.3) interfaced with CASCADE3 (version 3.2.2) [5], labeled MG5_aMC+CA3 (jj), is used with MEs computed at NLO for the process $pp \rightarrow jj$. The HERWIG6 [32] subtraction terms are used in MC@NLO [33, 34], since they are closest to the needs for applying PB-TMD parton densities, as described in Ref. [5]. The NLO PB-TMD set 2 [1] with $\alpha_S(m_Z) = 0.118$ is used. Multiparton interactions are not simulated in this approach.

- MADGRAPH5_aMC@NLO [4] (version 2.6.3) interfaced with CASCADE3, labeled MG5_aMC+CA3 (jjj) NLO, is used with MEs computed at NLO for the process $pp \rightarrow jjj$. The same PB-TMD distribution and parton shower calculation procedure as for MG5_aMC+CA3 (jj) are used.

In Table 1, the Monte Carlo event generators utilized in this analysis are summarized. Events generated by PYTHIA8, MADGRAPH+PY8, and HERWIG++ are passed through a full detector simulation based on GEANT4 [35]. The simulated events are reconstructed the same way as the observed data events.

Table 1: Description of the simulated samples used in the analysis.

Generator	PDF	ME	Tune
PYTHIA8 [23]	NNPDF 2.3 (LO) [25]	LO 2 \rightarrow 2	CUETP8M1 [24]
MADGRAPH+PY8 [4]	NNPDF 2.3 (LO) [25]	LO 2 \rightarrow 2, 3, 4	CUETP8M1 [24]
MADGRAPH+CA3 [4]	PB-TMD set 2 (NLO) [1]	LO 2 \rightarrow 2, 3, 4	—
HERWIG++ [26]	CTEQ6L1 (LO) [27]	LO 2 \rightarrow 2	CUETHppS1 [24]
MG5_aMC+Py8 (jj)	NNPDF 3.0 (NLO) [31]	NLO 2 \rightarrow 2	CUETP8M1 [24]
MG5_aMC+CA3 (jj)	PB-TMD set 2 (NLO) [1]	NLO 2 \rightarrow 2	—
MG5_aMC+CA3 (jjj)	PB-TMD set 2 (NLO) [1]	NLO 2 \rightarrow 3	—

4 Data analysis

The measured data samples recorded in 2016, corresponding to an integrated luminosity of 36.3 fb^{-1} , were collected with single-jet HLT. For each single-jet HLT at least one jet with p_T higher than the p_T^{HLT} trigger threshold is required. All triggers, except the one with the highest p_T^{HLT} threshold, were prescaled. We consider events only if the leading jet, reconstructed with the PF algorithm, can be matched with an HLT jet. In Table 2, the integrated luminosity \mathcal{L} for each trigger is shown. The trigger efficiency ($> 99.5\%$) is estimated using triggers with lower p_T^{HLT} thresholds; for the trigger with lowest p_T^{HLT} threshold a tag-and-probe [13] method is used to determine the p_T threshold. The trigger inefficiency due to prefireing (as discussed in Section 2) is included in the simulated event samples.

Table 2: The integrated luminosity for each trigger sample considered in this analysis with the p_T thresholds for HLT (PF) reconstruction.

p_T^{HLT} (GeV)	40	60	80	140	200	260	320	400	450
p_T^{PF} (GeV)	74	97	133	196	272	362	430	548	592
$\mathcal{L}(\text{pb}^{-1})$	0.267	0.726	2.76	24.2	103	594	1770	5190	36300

The jets are corrected using the JES correction procedure in CMS [20], and an additional smoothing procedure (described in Ref. [36]) is applied to the JES correction. The simulated samples are corrected to take into account the JER by spreading the p_T of the jets according to the resolution extracted from data. Jets reconstructed in regions of the detector corresponding to noisy towers in the calorimeters are excluded from the measurement.

The pileup profile used in simulation is corrected to reproduce the one in data.

4.1 Event selection

Each event is required to have a reconstructed PV. The PV must satisfy $|z_{\text{PV}}| < 24 \text{ cm}$ and $\rho_{\text{PV}} < 2 \text{ cm}$, where z_{PV} (ρ_{PV}) is the longitudinal (radial) distance from the nominal interaction point.

All events that contain jets clustered using the anti- k_T algorithm [17, 18] with a distance parameter of $R = 0.4$ and reconstructed with $|\eta| < 3.2$ and transverse momentum $p_T > 20$ GeV are preselected. From these events, the ones with at least a pair of jets with $p_{T1} > 200$ GeV, $p_{T2} > 100$ GeV and $|y^{1,2}| < 2.5$ are selected (events with one of the leading two jets with $|y| > 2.5$ are vetoed). Additional jets must have $p_T > 50$ GeV and $|y| < 2.5$. In addition, jets must satisfy quality criteria based on the jet constituents, in order to reject misidentified jets [37]. The selected events must have a missing transverse energy fraction smaller than 0.1 (more details in Sec. 4.3). The selection at particle-level includes only the p_T and $|y|$ constraints on the jets.

4.2 Observables and phase space

In the following, the observables will be described at particle-level. The particle-level is defined after all the partons have hadronized to form stable particles with a proper lifetime above 10 mm/c.

The exclusive jet multiplicity (N_{jets}) of up to 6 jets (inclusive for $N_{\text{jets}} \geq 7$), in three bins of p_{T1} ($200 < p_{T1} < 400$, $400 < p_{T1} < 800$, and $p_{T1} > 800$ GeV) and for three different regions in $\Delta\phi_{1,2}$ ($0 < \Delta\phi_{1,2} < 150$, $150 < \Delta\phi_{1,2} < 170$, $170 < \Delta\phi_{1,2} < 180^\circ$) is measured:

$$\frac{d\sigma_{\text{dijet}}}{dN_{\text{jets}}^i dp_{T1}^j d(\Delta\phi_{1,2})^k} \quad (1)$$

where i, j, k corresponds to the binning in N_{jets} , p_{T1} , and $\Delta\phi_{1,2}$.

In addition, the differential cross section as a function of the p_T of each of the four leading jets are measured:

$$\frac{d\sigma_{\text{pp} \rightarrow \text{jj}}}{dp_{T1}}, \quad \frac{d\sigma_{\text{pp} \rightarrow \text{jj}}}{dp_{T2}}, \quad \frac{d\sigma_{\text{pp} \rightarrow \text{jjj}}}{dp_{T3}}, \quad \frac{d\sigma_{\text{pp} \rightarrow \text{jjjj}}}{dp_{T4}}, \quad (2)$$

where $\sigma_{\text{pp} \rightarrow \text{jj}}$, $\sigma_{\text{pp} \rightarrow \text{jjj}}$, $\sigma_{\text{pp} \rightarrow \text{jjjj}}$ correspond to the dijet, three-jet, and four-jet cross sections in proton-proton collision.

4.3 Background treatment

To remove background contributions from $t\bar{t} + \text{jets}$, $W/Z + \text{jets}$, $Z \rightarrow \nu\bar{\nu}$ and $W \rightarrow l\nu$, events with $E_T^{\text{miss}} / \sum E_T > 0.1$ are rejected. The missing transverse energy is calculated from p_T^{miss} and the sum $\sum E_T$ runs over all PF objects in the event. Less than 1% of the events are rejected in the whole sample. For $N_{\text{jets}} = 2$ this constraint becomes important and the background contribution is reduced from 20% to the percent level for $p_{T1} > 800$ GeV in the low $\Delta\phi_{1,2}$. In Fig. 1, the measured fraction $E_T^{\text{miss}} / \sum E_T$ is compared with the simulation of signal and background processes in bins of $\Delta\phi_{1,2}$.

4.4 Correction for detector effects

The measured cross sections are corrected for misidentified events, detector resolution, and inefficiencies for comparison with particle-level predictions through the procedure of unfolding. A response matrix (RM) mapping the “true” distribution onto the measured one is constructed using simulated MC samples from PYTHIA8, MADGRAPH+PY8, and HERWIG++. The MADGRAPH+PY8 sample, which has the smallest statistical uncertainty, is used as default for constructing the RM, whereas the HERWIG++ and PYTHIA8 samples are used to investigate the model dependence. The RM is constructed by matching the detector and particle-level distributions. If events (or jets) cannot be matched, they contribute to the background or inefficiency

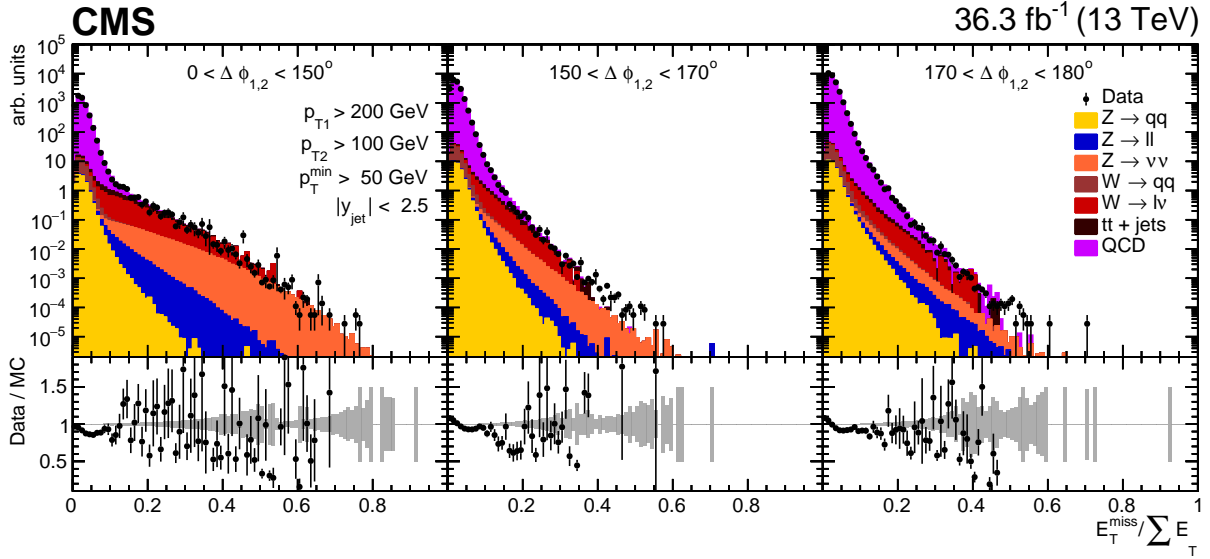


Figure 1: Distribution of $E_T^{\text{miss}} / \sum E_T$ for data and simulated jet production for three regions of $\Delta\phi_{1,2}$. Shown are the contributions from QCD, W/Z and $t\bar{t}$ events. The main contributions of events with large E_T^{miss} in the final state come from processes like $Z \rightarrow \nu\bar{\nu}$ and $W \rightarrow l\nu$. The data (MC prediction) statistical uncertainty is shown as a vertical line (grey shaded bar in the ratio).

distributions. For the jet multiplicity, the dijet system (leading and subleading jets) is matched if the jets coincide within $\Delta R < 0.2$ (half of the jet radius of $R = 0.4$). For the p_T distributions, jets are matched with $\Delta R < 0.2$, and from the matched candidates the one highest in p_T is selected (only events with at least two jets are considered in the matching). The TUNFOLD (version 17.9) package [38] is used to perform the unfolding.

The jet multiplicity is obtained by matrix inversion:

$$\mathbf{A}\alpha + \beta = \gamma \quad (3)$$

where $\gamma(\alpha)$ is the distribution at detector (particle) level, \mathbf{A} is the probability matrix (PM), and β is the contribution from background (or noise). The PM is obtained by normalizing the RM to the particle-level axis (row-by-row normalization), and describes the probability that a particle-level jet (or event) generated in a bin is reconstructed in (migrates to) another bin at detector-level. The condition number of the PM is defined as the ratio between the largest and smallest singular value of the matrix. The condition number of the PM for the jet multiplicity is 3.0, and matrix inversion is possible.

For the p_T distributions, the condition number of the PM is 4.9, and least-square minimisation is applied:

$$\chi^2 = \min_{\alpha} \left[(\gamma - \beta - \mathbf{A}\alpha)^T \mathbf{V}_{\gamma\gamma}^{-1} (\gamma - \beta - \mathbf{A}\alpha) \right], \quad (4)$$

where $\mathbf{V}_{\gamma\gamma}$ represents the statistical covariance matrix of γ and β , with twice the number of bins at detector level compared to particle-level. No additional regularization is needed.

In Fig. 2 and 3, the PMs are shown for the multiplicity distributions and the p_T distributions of the first four jets.

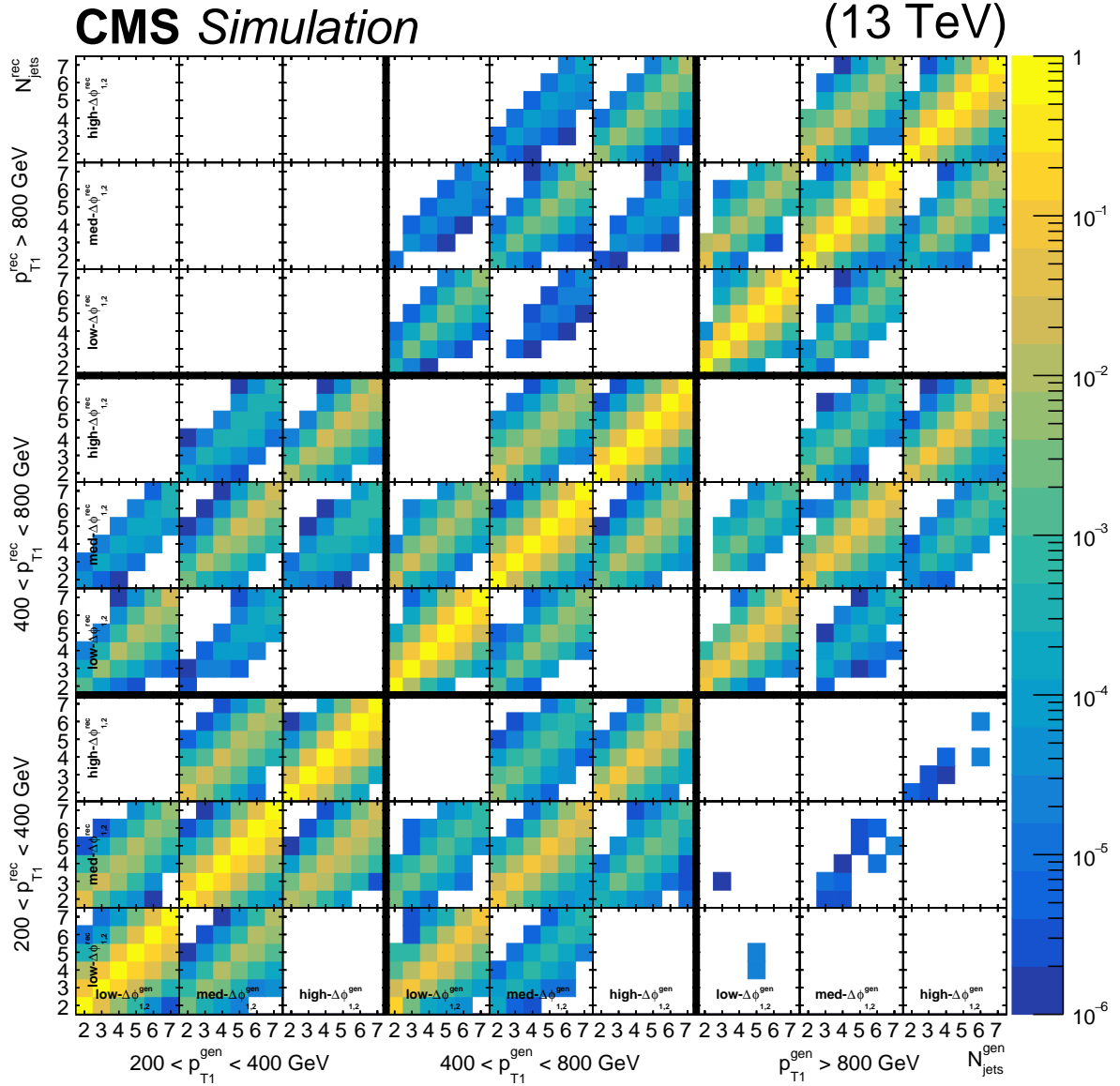


Figure 2: Probability matrix (condition number: 3.0) for the jet multiplicity distribution constructed with the MADGRAPH+PY8 sample. The global 3×3 sectors (separated by the thick black lines) correspond to the p_{T1} bins, indicated by the labels in the x (lower) and y (left) axes; the smaller 3×3 structures correspond to the $\Delta\phi_{1,2}$ bins, indicated in the leftmost row and lowest column, the x(y) axis of these $\Delta\phi_{1,2}$ cells corresponds to the jet multiplicity at particle (detector) level. The z axis covers a range from 10^{-6} to 1 indicating the probability of migrations from the particle-level bin to the corresponding detector-level bin.

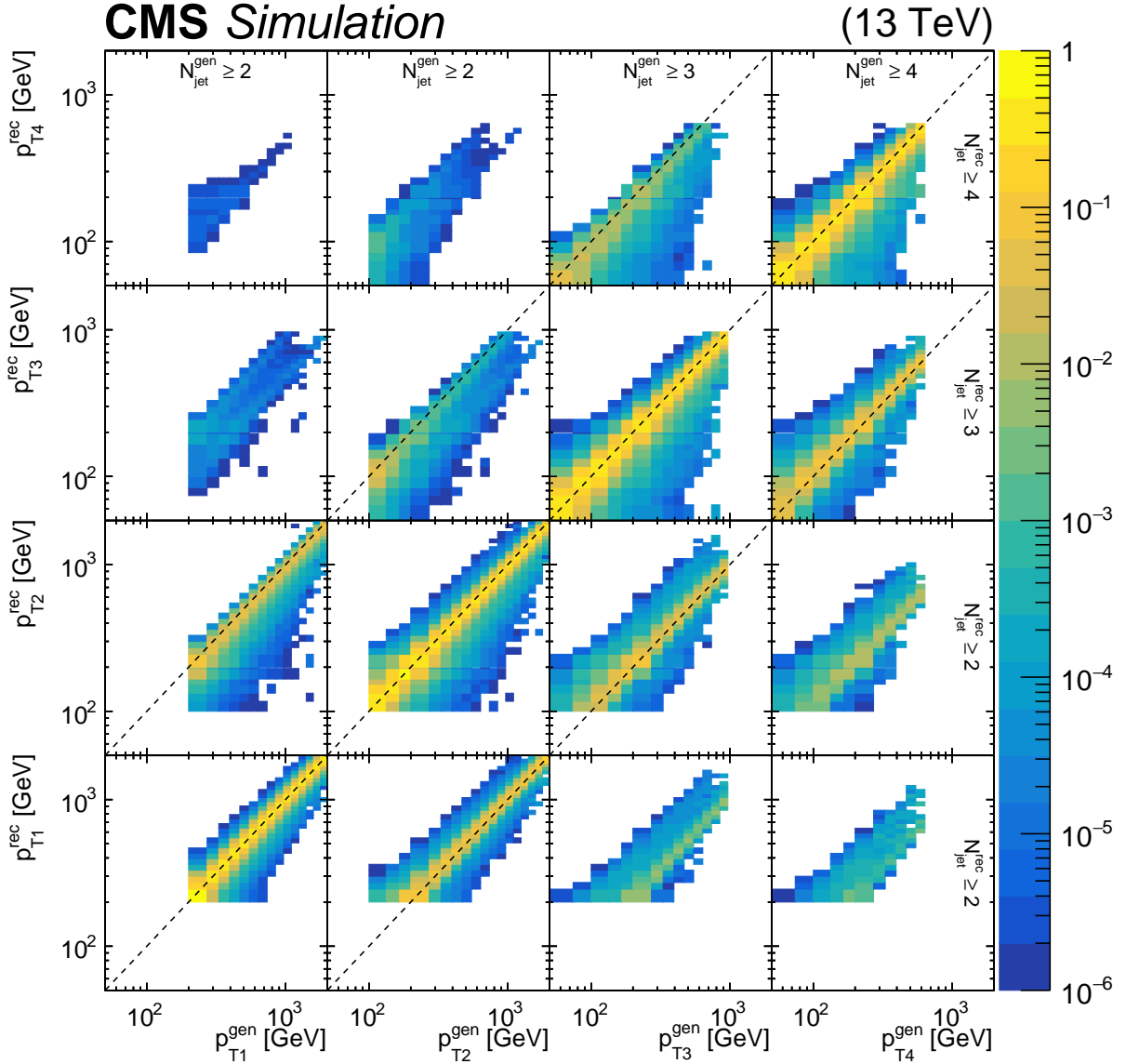


Figure 3: Probability matrix (condition number: 4.9) for the p_T of the four leading jets constructed with the MADGRAPH+PY8 sample. The global 4×4 sectors correspond to the p_T distributions each of the first four jets, the x axis corresponds to the particle (gen) level and y axis corresponds to the detector (rec) level. The z axis covers a range from 10^{-6} to 1 indicating the probability of migrations from the particle-level bin to the corresponding detector-level bin.

4.5 Uncertainties

The statistical uncertainties in the measured spectra and response matrices are propagated to the final results. In Fig. 4 and 5, the statistical correlations are shown for the jet multiplicity and for the p_T spectra of the four leading jets.

The systematic uncertainties originate from the following sources:

- JES: The JES uncertainty is estimated from variations of one standard deviation in the JES corrections applied to data (at detector-level) and repeating the whole unfolding procedure for each variation.
- JER: The JER uncertainty is estimated by varying the resolution by one standard deviation in the simulated sample, and repeating the unfolding for each variation.
- Integrated luminosity: The uncertainty in the integrated luminosity is 1.2% [39] and is applied as a global scaling factor to the cross section.
- Pileup: The pileup distribution in the simulated samples is reweighted to match that of the data. The corresponding uncertainty is estimated by varying the total inelastic cross section by $\pm 5\%$ [40], affecting the measurement by less than 1%.
- Trigger prefiring uncertainty: The trigger prefiring uncertainty is estimated by varying the correction applied to the simulated samples and repeating the unfolding for each variation, resulting in an uncertainty of 1 to 3%.
- Model uncertainty: The model uncertainty is estimated by varying the distributions of the factorization and renormalization scales in the MC sample such as to still describe the detector level distributions. Additionally background and inefficiencies are varied separately by 15%. The final uncertainty is the quadratic sum of each of the uncertainties. The model uncertainty, validated with the HERWIG++ and PYTHIA8 samples, ranges from 1 to 7%.

The total systematic uncertainty is obtained by adding all the systematic uncertainties in quadrature, assuming independent sources.

In Fig. 6, the relative uncertainties for the jet multiplicity in bins of p_{T1} and $\Delta\phi_{1,2}$ are shown. The dominant uncertainty is JES. The total statistical uncertainty (stat. unc.) is mainly driven by the limited event counts in data. The total experimental uncertainty (Total) is typically about 10 to 15%.

In Fig. 7, the relative uncertainties as a function of the jet p_T for the four leading jets are shown. The dominant uncertainty is JES. The measurement is limited by the systematic uncertainty and the total experimental uncertainty ranges from 5 to 10%.

5 Results

The phase space of the measurements at particle-level (particles with a proper lifetime above 10 mm/c) is defined by jets clustered using the anti- k_T algorithm [17, 18] with a distance parameter of $R = 0.4$ within $|y| < 3.2$. Events are selected if the two highest p_T jets with $p_{T1} > 200$ GeV, $p_{T2} > 100$ GeV have $|y| < 2.5$ (i.e., events are not counted where one of the leading jets has $|y| > 2.5$). For the additional jets $p_T > 50$ GeV and $|y| < 2.5$ is required. All predictions (LO and NLO) are normalized to the measured dijet cross section in the measurement phase space, with the normalization factors explicitly given in the figures.

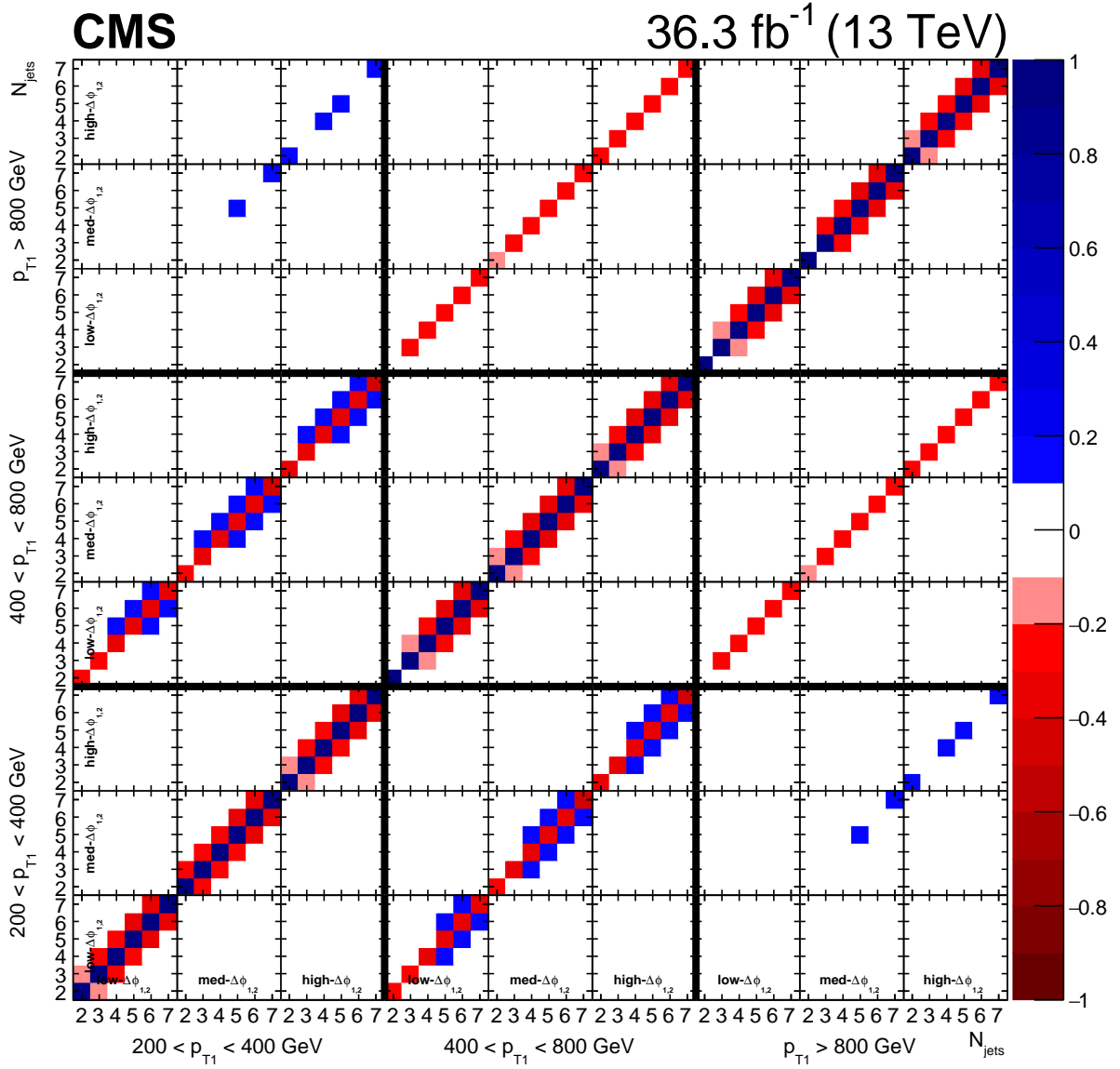


Figure 4: Correlation matrix at the particle-level for the jet multiplicity distribution. It contains contributions from the data and from the limited-size MADGRAPH+PY8 sample. The global 3×3 sectors (separated by the thick black lines) correspond to the p_{T1} bins, indicated by the labels next to the x (lower) and y (left) axes; the smaller 3×3 structures correspond to the $\Delta\phi_{1,2}$ bins, indicated in the leftmost row and lowest column, the x and y axes correspond to the jet multiplicity. The z axis covers a range from -1 to 1 indicating the correlations in blue shades and anticorrelations in red shades, the values between -0.1 and 0.1 are represented in white.

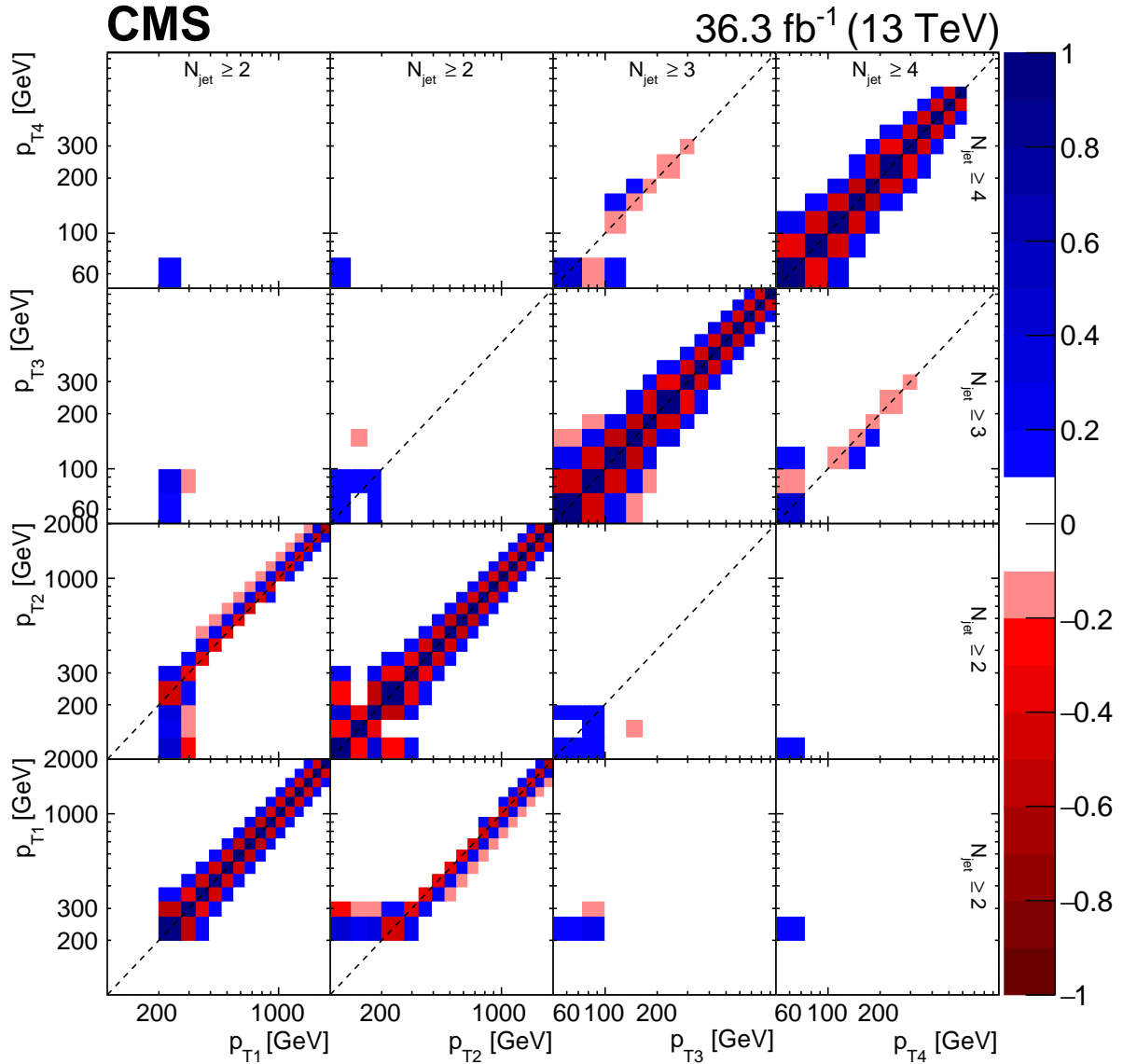


Figure 5: Correlation matrix for the particle-level p_T of the four leading jets. It contains contributions from the data and from the limited-size MADGRAPH+PY8 sample. Here each one of the 4×4 sectors corresponds to one of the p_T spectra measured, indicated by the x and y axis labels. The z axis covers a range from -1 to 1 indicating the correlations in blue shades and anticorrelations in red shades, the values between -0.1 and 0.1 are represented in white.

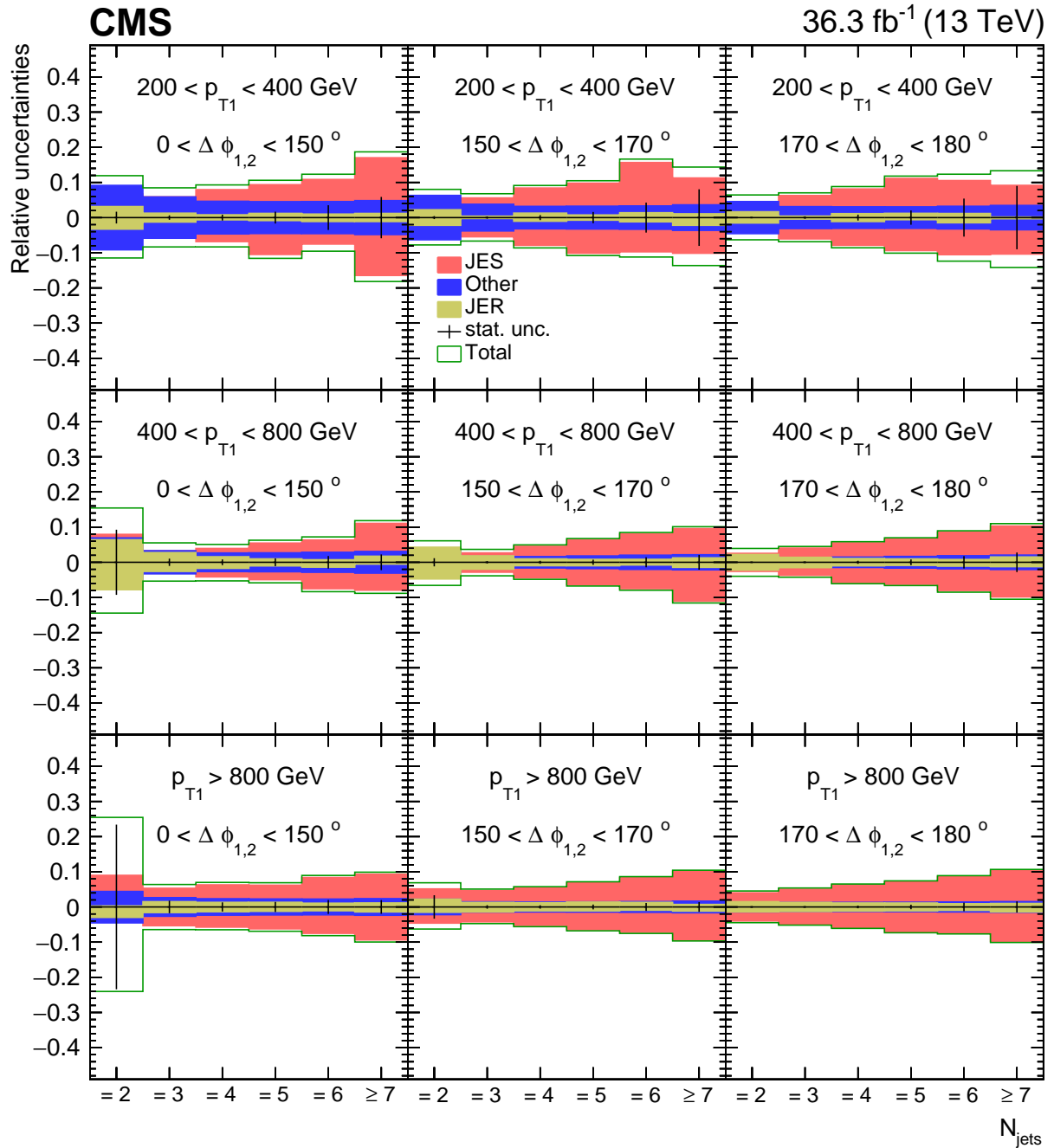


Figure 6: Relative uncertainties for JES, JER, “Other” and total statistical uncertainty for the jet multiplicity distribution in bins of p_{T1} and $\Delta\phi_{1,2}$. Here “Other” indicates luminosity, pileup, preflring, and model uncertainty.

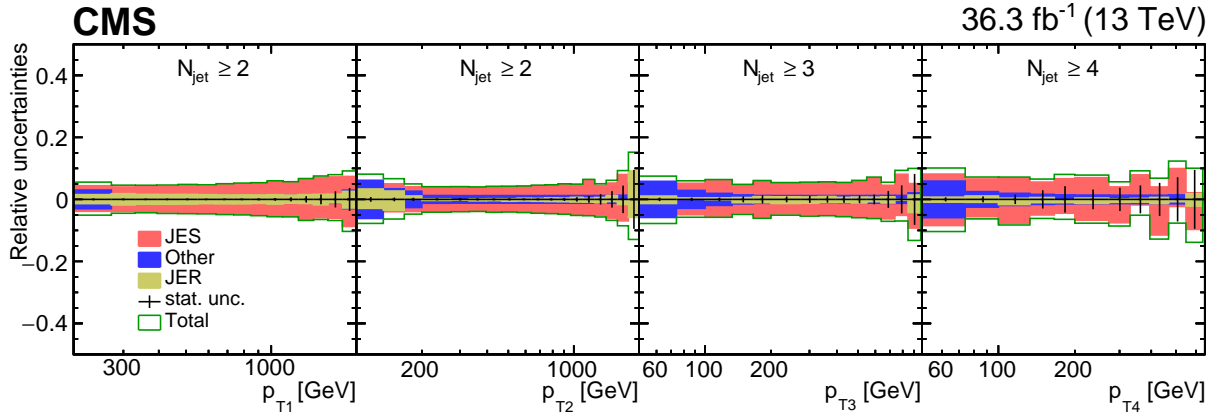


Figure 7: Relative uncertainties for JES, JER, “Other” and total statistical uncertainty for the p_T distributions of the four leading jets. Here “Other” indicates luminosity, pileup, prefiring, and model uncertainty.

5.1 Jet multiplicity distribution

The multiplicity of jets with $p_T > 50$ GeV in $|y| < 2.5$ is measured for various regions of the transverse momentum of the leading jet, p_{T1} , and the azimuthal angle $\Delta\phi_{1,2}$ between the two leading jets as shown in Fig. 8.

As a characterization of the jet multiplicity we compare the production rate for 3 jets with the one for 7 jets. In the region of low p_{T1} ($200 < p_{T1} < 400$ GeV), a large number of additional jets is observed at low $\Delta\phi_{1,2}$ ($0 < \Delta\phi_{1,2} < 150^\circ$), the production rate between 3 and 7 jets changes by two orders of magnitude. In the large- $\Delta\phi_{1,2}$ region ($170 < \Delta\phi_{1,2} < 180^\circ$), where the leading jets are nearly back-to-back, the production rate for 3 to 7 jets changes by three orders of magnitude. We note that even in this back-to-back region a large number of additional jets are observed that do not contribute significantly to the momentum imbalance of the two leading jets.

In the region of large p_{T1} ($p_{T1} > 800$ GeV), we observe that the rate of additional jets at low $\Delta\phi_{1,2}$ is essentially constant and the rate between 3 and 7 jets only shows small changes, indicating that many jets participate in the compensation of the $\Delta\phi_{1,2}$ decorrelation. In the large- $\Delta\phi_{1,2}$ region ($170 < \Delta\phi_{1,2} < 180^\circ$), the rate between 3 and 7 jets changes by less than 2 orders of magnitude, in contrast to the low- p_{T1} region. A multiplicity of more than two or three additional jets at large p_{T1} is observed in all regions of $\Delta\phi_{1,2}$.

In Fig. 8, predictions from the LO $2 \rightarrow 2$ generators PYTHIA 8 and HERWIG++ including parton showering and multiparton interactions are shown. The shape of the prediction coming from PYTHIA 8 is different from what is observed in the measurement. The shape of the prediction from HERWIG++ agrees rather well with the measurement, especially in the large $\Delta\phi_{1,2}$ region. The difference between PYTHIA 8 and HERWIG++ in jet multiplicity comes from the different treatment of the parton shower. In addition the predictions from MADGRAPH+PY8 and MADGRAPH+CA3 with additional noncollinear high- p_T partons, supplemented with different parton showering approaches and multiparton interactions are shown. The prediction from MADGRAPH+PY8 does not agree in shape with the measurement, whereas the MADGRAPH+CA3 prediction does, similarly to the case of HERWIG++.

The calculations with NLO MEs matched with parton shower compared with the measurements are shown in Fig. 9. The uncertainty bands of the predictions come from the variation of the factorization and renormalization scales by a factor of two up and down, avoiding the

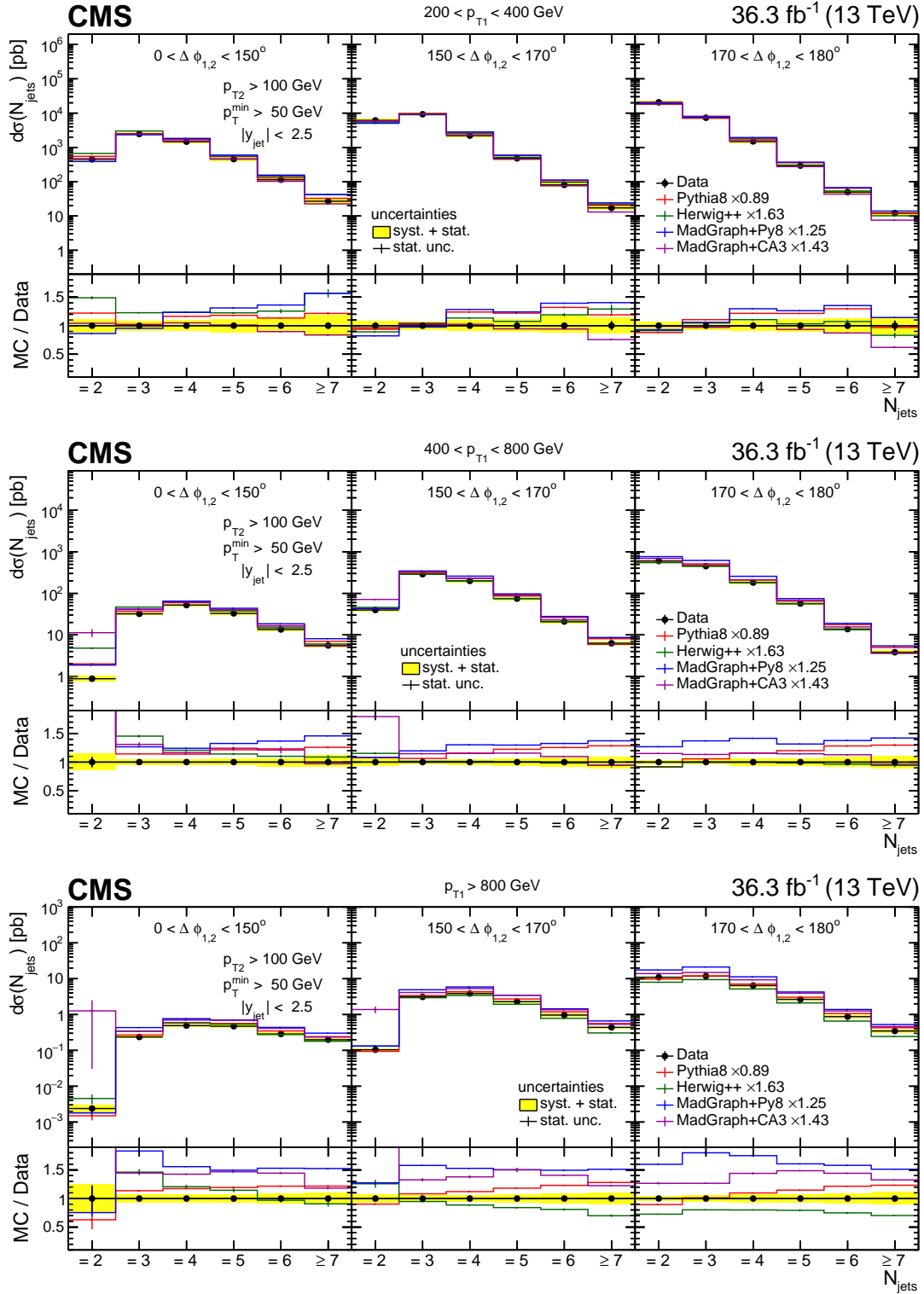


Figure 8: Differential cross section as a function of the exclusive jet multiplicity (inclusive for 7 jets) in bins of p_{T1} and $\Delta\phi_{1,2}$. The data are compared with LO predictions of PYTHIA 8, HERWIG++, MADGRAPH+PY8 and MADGRAPH+CA3. The predictions are normalized to the measured dijet cross section using the scaling factors shown in the legend. The vertical error bars correspond to the statistical uncertainty, the yellow band shows the total experimental uncertainty.

largest scale differences. The normalization of the MG5_aMC+Py8 (jj) calculation is in reasonable agreement with the measured cross section even for three jets. For higher jet multiplicities the prediction falls below the measurement. MG5_aMC+CA3 (jj) predicts a smaller cross section for more than three jets compared with the measurement. The MG5_aMC+CA3 (jjj) NLO calculation (using the same normalization factor as for MG5_aMC+CA3 (jj)) predicts a larger three- and four-jet cross section, whereas the higher jet multiplicities are still underestimated.

5.2 Transverse momenta of the four leading jets

The measured differential jet cross section as a function of the jet transverse momentum, p_T , for the four leading p_T jets is shown in Fig. 10 and compared with the predictions of PYTHIA 8 and MG5_aMC+Py8 (jj). The p_T values of the two leading- p_T jets reaches up to 2 TeV and the third and fourth jets p_T reaches about 1 TeV. We observe that the shape of the p_T spectrum for the third and fourth leading jets is qualitatively similar to the one of the two leading jets, whereas the cross section is different. The rise of the cross section for the second jet between 100 GeV and 200 GeV is a consequence of the higher p_T requirement ($p_{T1} > 200$ GeV) applied to the leading jet in the event selection.

In Fig. 11, the measured differential cross section as a function of the p_T for the four leading jets is shown and compared with LO predictions (using the same normalization factors as in Fig. 8). Only the prediction of PYTHIA 8 is able to describe reasonably well the measurement in shape, except for the region $p_{T2} < 200$ GeV. The shape of the third and fourth jet distributions is not well described, and PYTHIA 8 overestimates the rate by up to 30%. The predictions from HERWIG++ are not in agreement in shape and rate with the measurements, the differences are up to 50% for the leading and subleading jets at large p_T . The prediction from MADGRAPH+PY8 gives a significantly different shape for the p_T spectrum for the first 3 jets. MADGRAPH+CA3 gives a significant improvement in the description of the shape of the p_T distribution for the three leading jets, whereas the description of the distribution of the fourth jet is similar to the one with MADGRAPH+PY8.

The predictions obtained with NLO MEs are shown in Fig. 12 using the same normalization factors as in Fig. 9. The uncertainty bands of the predictions come from the variation of the factorization and renormalization scales by a factor of two up and down, avoiding the largest scale differences. The predictions of MG5_aMC+Py8 (jj) and MG5_aMC+CA3 (jj) describe the normalization and the shape of the first three jets rather well, whereas for the fourth jet (which comes from the parton shower) falls below the measurement by 20–30%. The prediction of MG5_aMC+CA3 (jjj) describes the third and fourth jets rather well within uncertainties (predictions for the first and second jet are meaningless for MG5_aMC+CA3 (jjj) and therefore not shown). This is the first time that calculations using PB-TMDs together with the calculation of the MEs in the MC@NLO frame are compared with jet measurements over a wide range in transverse momentum and jet multiplicities.

6 Summary

A study of multijet events has been performed in proton-proton collisions at a center-of-mass energy of 13 TeV using data collected with the CMS detector corresponding to an integrated luminosity of 36.3 fb^{-1} . The measurements are performed by selecting a dijet system containing a jet with $p_T > 200$ GeV and a subleading jet with $p_T > 100$ GeV within $|y| < 2.5$.

For the first time, the jet multiplicity in bins of the leading jet p_T and the azimuthal angle difference between the two leading jets, $\Delta\phi_{1,2}$, is measured. The jet multiplicity distributions

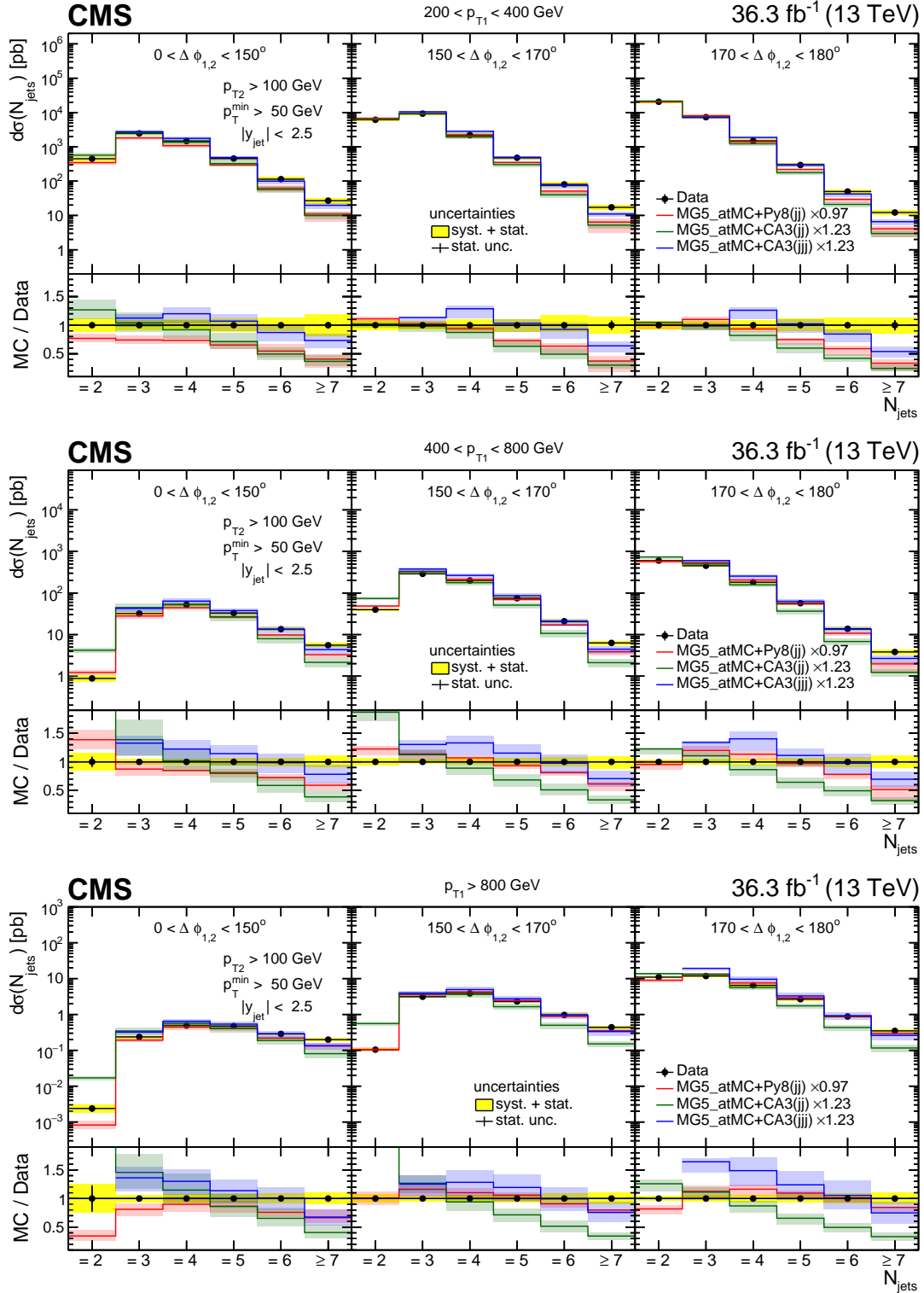


Figure 9: Differential cross section as a function of the exclusive jet multiplicity (inclusive for 7 jets) in bins of p_{T1} and $\Delta\phi_{1,2}$. The data are compared with NLO dijet predictions MG5.aMC+Py8 (jj) and MG5.aMC+CA3 (jj) as well as the NLO three-jet prediction of MG5.aMC+CA3 (jjj). The vertical error bars correspond to the statistical uncertainty, the yellow band shows the total experimental uncertainty. The shaded bands show the uncertainty from a variation of the renormalization and factorization scales. The predictions are normalized to the measured inclusive dijet cross section using the scaling factors shown in the legend.

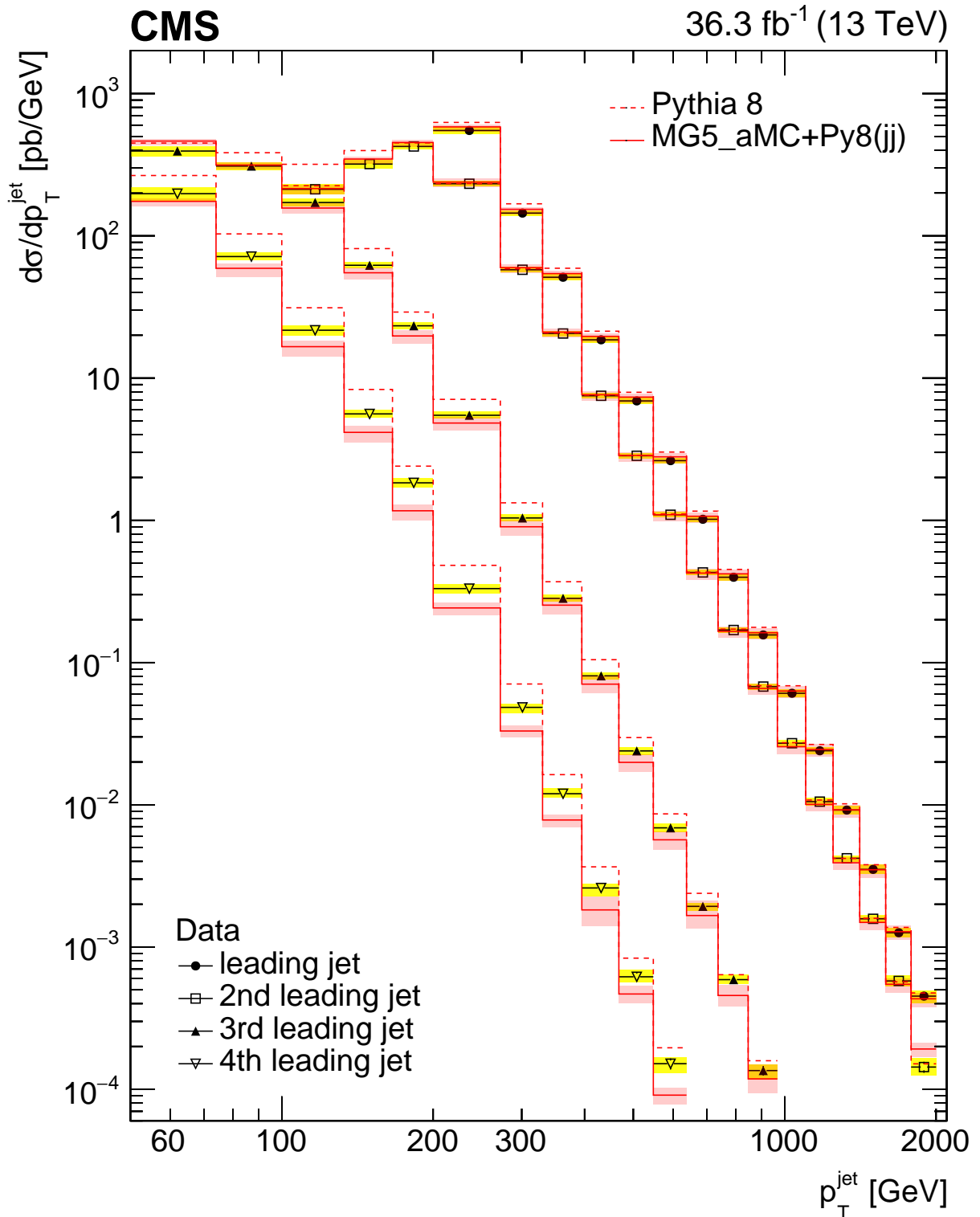


Figure 10: Transverse momenta of the four leading jets, with the yellow band representing the total experimental uncertainty. The data are compared with LO (PYTHIA 8) and NLO (MG5.aMC+Py8) predictions. The red band in the NLO prediction represents the renormalization and factorization scale uncertainty.

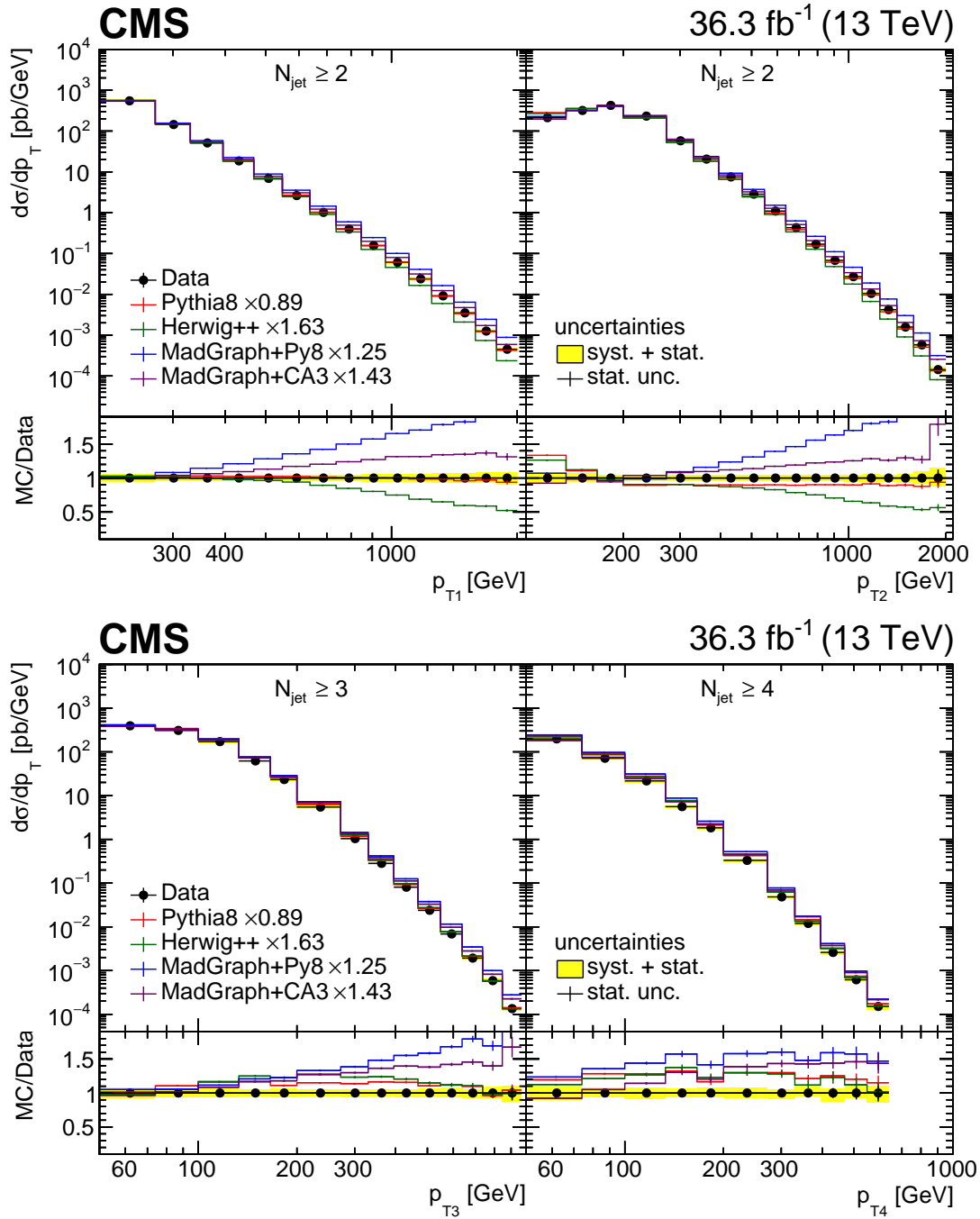


Figure 11: Transverse momentum distributions of the four leading jets. The transverse momentum of the leading and subleading (third and fourth leading) p_T jets from left to right is shown in the upper (lower) figure. The data are compared with LO predictions of PYTHIA 8, HERWIG++, MADGRAPH+PY8 and MADGRAPH+CA3. The predictions are normalized to the measured dijet cross section using the scaling factors shown in the legend. The vertical error bars correspond to the statistical uncertainty, the yellow band shows the total experimental uncertainty.

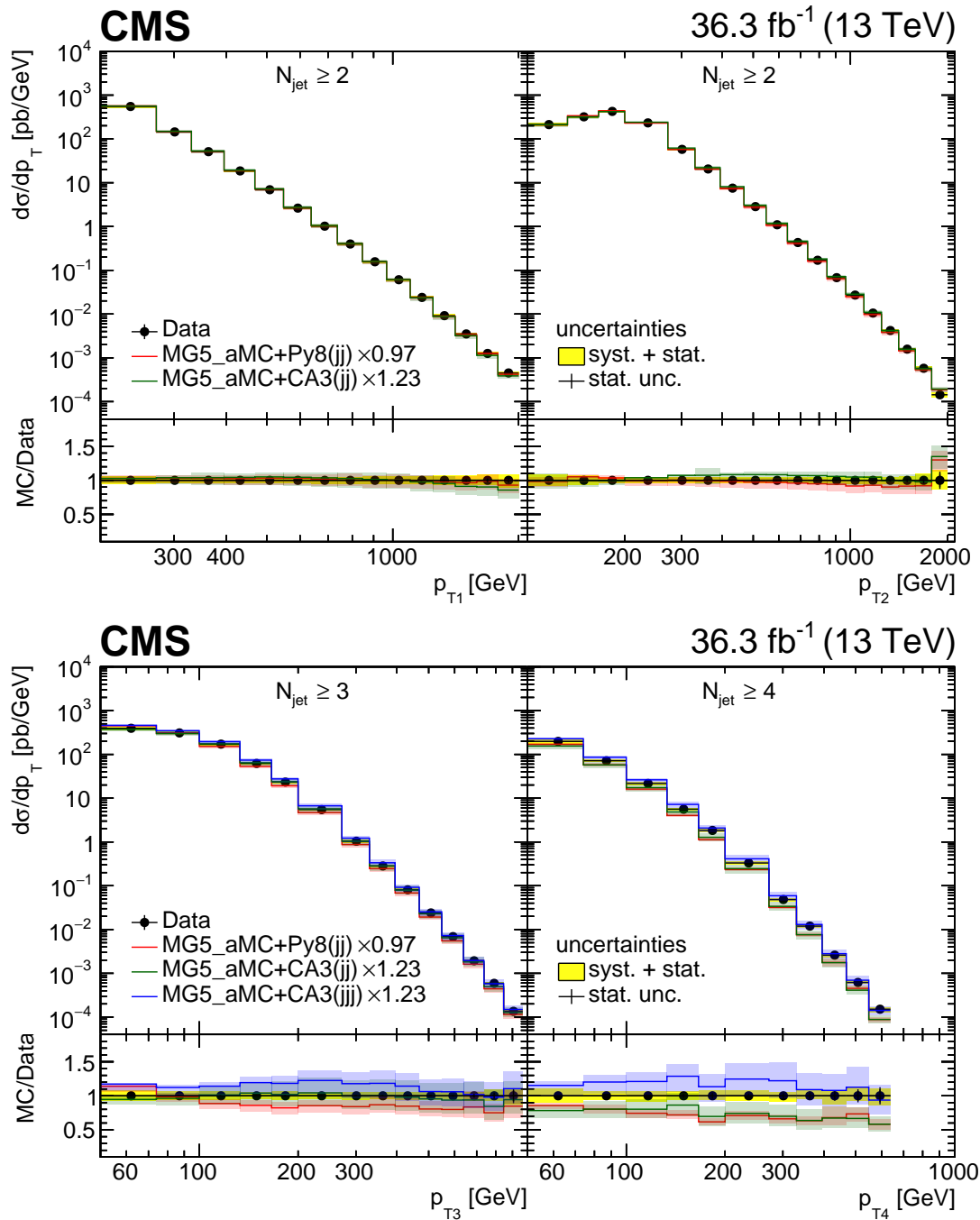


Figure 12: Transverse momentum distributions of the four leading jets. The transverse momentum of the leading and subleading (third and fourth leading) p_T jets from left to right is shown in the upper (lower) figure. The data are compared with NLO predictions MG5_aMC+Py8 (jj) and MG5_aMC+CA3 (jj) as well as the NLO three-jet prediction of MG5_aMC+CA3 (jjj). The vertical error bars correspond to the statistical uncertainty, and the yellow band to total uncertainty of the measurement. The bands show the uncertainty from a variation of the renormalization and factorization scales. The predictions are normalized to the measured dijet cross section using the scaling factors shown in the legend.

show that even in the back-to-back region of the dijet system, up to seven jets are measurable. The differential production cross sections are measured for the highest p_T jets up to the TeV scale.

The measurement of the differential cross section as a function of the jet p_T for the four highest p_T jets is an important reference for standard model multijet cross section calculations, and especially for the simulations including parton showers for higher jet multiplicity.

The measured multiplicity distribution of jets with $p_T > 50 \text{ GeV}$ and $|y| < 2.5$ is not well described by the leading order MADGRAPH+PYTHIA 8 simulation. However, in the back-to-back region HERWIG++ and MADGRAPH+CASCADE3 provide a better description of the shape of the jet multiplicity. The measured differential cross section as a function of the transverse momentum of the four leading p_T jets is not described by any of the LO predictions either in normalization or in shape. However, MADGRAPH+CASCADE3 describes the shape of the distribution better than MADGRAPH+PYTHIA 8.

The predictions using dijet NLO matrix elements, MG5_AMC+PYTHIA 8 (jj) and MG5_AMC+CASCADE3 (jj) describe the lower multiplicity regions, as well as the transverse momenta of the leading jets, reasonably well. The three-jet NLO calculation MG5_AMC+CASCADE3 (jjj) describes very well the cross section of the third and fourth jets.

The measurements presented here provide stringent tests of theoretical predictions in the perturbative high- p_T and high-jet multiplicity regions. Although the higher jet multiplicities are not described with either parton shower approach, it is interesting that the lower jet multiplicity cross section is described satisfactorily with NLO dijet calculations supplemented with PB-TMDs and TMD parton shower with fewer tunable parameters than in the case with conventional parton showers.

The measured observables and its statistical correlations are provided in HEPData [41] as tabulated results.

References

- [1] A. Bermudez Martinez et al., “Collinear and TMD parton densities from fits to precision DIS measurements in the parton branching method”, *Phys. Rev. D* **99** (2019) 074008, doi:10.1103/PhysRevD.99.074008, arXiv:1804.11152.
- [2] F. Hautmann et al., “Soft-gluon resolution scale in QCD evolution equations”, *Phys. Lett. B* **772** (2017) 446, doi:10.1016/j.physletb.2017.07.005, arXiv:1704.01757.
- [3] F. Hautmann et al., “Collinear and TMD quark and gluon densities from parton branching solution of QCD evolution equations”, *JHEP* **01** (2018) 070, doi:10.1007/JHEP01(2018)070, arXiv:1708.03279.
- [4] J. Alwall et al., “The automated computation of tree-level and next-to-leading order differential cross sections, and their matching to parton shower simulations”, *JHEP* **07** (2014) 079, doi:10.1007/JHEP07(2014)079, arXiv:1405.0301.
- [5] S. Baranov et al., “CASCADE3 A Monte Carlo event generator based on TMDs”, *Eur. Phys. J. C* **81** (2021) 425, doi:10.1140/epjc/s10052-021-09203-8, arXiv:2101.10221.
- [6] D0 Collaboration, “Measurement of dijet azimuthal decorrelations at central rapidities in $p\bar{p}$ collisions at $\sqrt{s} = 1.96$ TeV”, *Phys. Rev. Lett.* **94** (2005) 221801, doi:10.1103/PhysRevLett.94.221801, arXiv:hep-ex/0409040.
- [7] D0 Collaboration, “Measurement of the combined rapidity and p_T dependence of dijet azimuthal decorrelations in $p\bar{p}$ collisions at $\sqrt{s} = 1.96$ TeV”, *Phys. Lett. B* **721** (2013) 212, doi:10.1016/j.physletb.2013.03.029, arXiv:1212.1842.
- [8] ATLAS Collaboration, “Measurement of dijet azimuthal decorrelations in pp collisions at $\sqrt{s} = 7$ TeV”, *Phys. Rev. Lett.* **106** (2011) 172002, doi:10.1103/PhysRevLett.106.172002, arXiv:1102.2696.
- [9] CMS Collaboration, “Dijet azimuthal decorrelations in pp collisions at $\sqrt{s} = 7$ TeV”, *Phys. Rev. Lett.* **106** (2011) 122003, doi:10.1103/PhysRevLett.106.122003, arXiv:1101.5029.
- [10] CMS Collaboration, “Measurement of dijet azimuthal decorrelation in pp collisions at $\sqrt{s} = 8$ TeV”, *Eur. Phys. J. C* **76** (2016) 536, doi:10.1140/epjc/s10052-016-4346-8, arXiv:1602.04384.
- [11] CMS Collaboration, “Azimuthal correlations for inclusive 2-jet, 3-jet, and 4-jet events in pp collisions at $\sqrt{s} = 13$ TeV”, *Eur. Phys. J. C* **78** (2018) 566, doi:10.1140/epjc/s10052-018-6033-4, arXiv:1712.05471.
- [12] CMS Collaboration, “Azimuthal separation in nearly back-to-back jet topologies in inclusive 2- and 3-jet events in pp collisions at $\sqrt{s} = 13$ TeV”, *Eur. Phys. J. C* **79** (2019) 773, doi:10.1140/epjc/s10052-019-7276-4, arXiv:1902.04374.
- [13] CMS Collaboration, “Performance of the CMS Level-1 trigger in proton-proton collisions at $\sqrt{s} = 13$ TeV”, *JINST* **15** (2020) P10017, doi:10.1088/1748-0221/15/10/P10017, arXiv:2006.10165.
- [14] CMS Collaboration, “The CMS trigger system”, *JINST* **12** (2017) P01020, doi:10.1088/1748-0221/12/01/P01020, arXiv:1609.02366.

-
- [15] CMS Collaboration, “Particle-flow reconstruction and global event description with the cms detector”, *JINST* **12** (2017) P10003, doi:10.1088/1748-0221/12/10/P10003, arXiv:1706.04965.
- [16] CMS Collaboration, “Technical proposal for the Phase-II upgrade of the Compact Muon Solenoid”, CMS Technical Proposal CERN-LHCC-2015-010, CMS-TDR-15-02, 2015.
- [17] M. Cacciari, G. P. Salam, and G. Soyez, “The anti- k_T jet clustering algorithm”, *JHEP* **04** (2008) 063, doi:10.1088/1126-6708/2008/04/063, arXiv:0802.1189.
- [18] M. Cacciari, G. P. Salam, and G. Soyez, “FastJet user manual”, *Eur. Phys. J. C* **72** (2012) 1896, doi:10.1140/epjc/s10052-012-1896-2, arXiv:1111.6097.
- [19] CMS Collaboration, “Pileup Removal Algorithms”, CMS Physics Analysis Summary CMS-PAS-JME-14-001, 2014.
- [20] CMS Collaboration, “Jet energy scale and resolution in the CMS experiment in pp collisions at 8 TeV”, *JINST* **12** (2017) P02014, doi:10.1088/1748-0221/12/02/P02014, arXiv:1607.03663.
- [21] CMS Collaboration, “Performance of missing transverse momentum reconstruction in proton-proton collisions at $\sqrt{s} = 13$ TeV using the CMS detector”, *JINST* **14** (2019) P07004, doi:10.1088/1748-0221/14/07/P07004, arXiv:1903.06078.
- [22] CMS Collaboration, “The CMS experiment at the CERN LHC”, *JINST* **3** (2008) S08004, doi:10.1088/1748-0221/3/08/S08004.
- [23] T. Sjöstrand et al., “An introduction to PYTHIA 8.2”, *Comput. Phys. Commun.* **191** (2015) 159, doi:10.1016/j.cpc.2015.01.024, arXiv:1410.3012.
- [24] CMS Collaboration, “Event generator tunes obtained from underlying event and multiparton scattering measurements”, *Eur. Phys. J. C* **76** (2016) 155, doi:10.1140/epjc/s10052-016-3988-x, arXiv:1512.00815.
- [25] NNPDF Collaboration, “Unbiased global determination of parton distributions and their uncertainties at NNLO and at LO”, *Nucl. Phys. B* **855** (2012) 153, doi:10.1016/j.nuclphysb.2011.09.024, arXiv:1107.2652.
- [26] M. Bahr et al., “Herwig++ physics and manual”, *Eur. Phys. J. C* **58** (2008) 639, doi:10.1140/epjc/s10052-008-0798-9, arXiv:0803.0883.
- [27] J. Pumplin et al., “New generation of parton distributions with uncertainties from global QCD analysis”, *JHEP* **07** (2002) 012, doi:10.1088/1126-6708/2002/07/012, arXiv:hep-ph/0201195.
- [28] J. Alwall et al., “Comparative study of various algorithms for the merging of parton showers and matrix elements in hadronic collisions”, *Eur. Phys. J. C* **53** (2008) 473, doi:10.1140/epjc/s10052-007-0490-5, arXiv:0706.2569.
- [29] A. Bermudez Martinez, F. Hautmann, and M. L. Mangano, “TMD evolution and multi-jet merging”, *Phys. Lett. B* **822** (2021) 136700, doi:10.1016/j.physletb.2021.136700, arXiv:2107.01224.
- [30] T. Sjöstrand, S. Mrenna, and P. Skands, “PYTHIA 6.4 physics and manual”, *JHEP* **05** (2006) 026, doi:10.1088/1126-6708/2006/05/026, arXiv:hep-ph/0603175.

- [31] NNPDF Collaboration, “Parton distributions for the LHC Run II”, *JHEP* **04** (2015) 040, doi:10.1007/JHEP04(2015)040, arXiv:1410.8849.
- [32] G. Corcella et al., “HERWIG 6: An event generator for hadron emission reactions with interfering gluons (including supersymmetric processes)”, *JHEP* **01** (2001) 010, doi:10.1088/1126-6708/2001/01/010, arXiv:hep-ph/0011363.
- [33] S. Frixione, P. Nason, and B. R. Webber, “Matching NLO QCD and parton showers in heavy flavor production”, *JHEP* **08** (2003) 007, doi:10.1088/1126-6708/2003/08/007, arXiv:hep-ph/0305252.
- [34] S. Frixione and B. R. Webber, “Matching NLO QCD computations and parton shower simulations”, *JHEP* **06** (2002) 029, doi:10.1088/1126-6708/2002/06/029, arXiv:hep-ph/0204244.
- [35] GEANT4 Collaboration, “GEANT4 – a simulation toolkit”, *Nucl. Instrum. Meth. A* **506** (2003) 250, doi:10.1016/S0168-9002(03)01368-8.
- [36] CMS Collaboration, “Measurement and QCD analysis of double-differential inclusive jet cross sections in proton-proton collisions at $\sqrt{s} = 13$ TeV”, *JHEP* **02** (2022) 142, doi:10.1007/JHEP02(2022)142, arXiv:2111.10431.
- [37] CMS Collaboration, “Jet algorithms performance in 13 TeV data”, CMS Physics Analysis Summary CMS-PAS-JME-16-003, CERN, Geneva, 2017.
- [38] S. Schmitt, “TUnfold: an algorithm for correcting migration effects in high energy physics”, *JINST* **7** (2012) T10003, doi:10.1088/1748-0221/7/10/T10003, arXiv:1205.6201.
- [39] CMS Collaboration, “Precision luminosity measurement in proton-proton collisions at $\sqrt{s} = 13$ TeV in 2015 and 2016 at CMS”, *Eur. Phys. J. C* **81** (2021) 800, doi:10.1140/epjc/s10052-021-09538-2, arXiv:2104.01927.
- [40] CMS Collaboration, “Measurement of the inelastic proton-proton cross section at $\sqrt{s} = 13$ TeV”, *JHEP* **07** (2018) 161, doi:10.1007/JHEP07(2018)161, arXiv:1802.02613.
- [41] HEPData record for this analysis, 2022. doi:10.17182/hepdata.133279.